

**Spatially adaptive estimation of multi-layer soil temperature at a daily time-step
across China during 2010-2020**

Xuetong Wang^{1, 2}, Liang He^{3, *}, Peng Li^{1, 2}, Jiageng Ma⁴, Yu Shi⁵, Qi Tian^{1, 2}, Gang Zhao^{2, 6}, Jianqiang He⁷, Hao Feng², Hao Shi^{8, 9, *}, Qiang Yu^{2, *}

¹ College of Natural Resources and Environment, Northwest A&F University, Yangling 712100, China

² State Key Laboratory of Soil and Water Conservation and Desertification Control, Northwest A&F University, Yangling 712100, China

³ National Meteorological Center, Beijing, 100081, China

⁴ Key Laboratory of Ecosystem Network Observation and Modeling, Institute of Geographic Sciences and Natural Resources Research, Chinese Academy of Sciences, Beijing 100101, PR China

⁵ Institute of Carbon Neutrality, Sino-French Institute for Earth System Science, College of Urban and Environmental Sciences, Peking University, Beijing 100871, China

⁶ College of Soil and Water Conservation Science and Engineering, Northwest A&F University, Yangling, Shaanxi, 712100, China

⁷ Key Laboratory for Agricultural Soil and Water Engineering in Arid Area of Ministry of Education, Northwest A&F University, Yangling 712100, China

⁸ State Key Laboratory for Ecological Security of Regions and Cities, Research Center for Eco-Environmental Sciences, Chinese Academy of Sciences, Beijing, 100085, China

⁹ College of Resources and Environment, University of Chinese Academy of Sciences, Beijing, 100049, China

Correspondence:

Liang He (heliang_hello@163.com)

Hao Shi (haoshi@rcees.ac.cn)

Qiang Yu (yuq@nwafu.edu.cn)

Abstract

Soil temperature (T_s) is critical in regulating agricultural production, ecosystem functions, hydrological cycling and climate dynamics. However, the inherent spatial and temporal heterogeneity of soil thermal regimes constitutes a persistent challenge in obtaining high-resolution, continuous gridded T_s datasets along vertical profiles. To address this issue, we propose a spatially adaptive layer-cascading Extreme Gradient Boosting (XGBoost) algorithm to generate daily multi-layer T_s data (0, 5, 10, 15, 20, and 40 cm) at a spatial resolution of 1 km in China from 2010 to 2020. The methodology dynamically partitions non-uniformly distributed measuring sites (2,093 sites across the country) to quadtrees and incorporates thermal coupling effects propagated between neighbor soil layers. Multi-source data, including satellite retrievals of land surface temperature and vegetation index, and ERA5 reanalysis climate variables were used as inputs. Validation using spatial block cross-validation and independent flux tower observations demonstrated the robustness and accuracy of the product. It is noted the model's performance was lower in summers and winters than in springs and autumns. Compared to existing global or regional T_s products, the dataset developed here is characterized by its fine spatio-temporal patterns and high reliability, enabling it to provide supports for precision agriculture, ecosystem modeling and understanding climate-land feedback. Free access to the dataset can be found at <https://doi.org/10.11888/Terre.tpdc.302333> (Wang et al., 2025b).

Key words: Soil temperature, spatially adaptive, machine learning, multi-source data

30 **1. Introduction**

Soil temperature (T_s) is a critical driver of ecosystem dynamics, influencing nearly all physical, chemical, and biological processes (Bayatvarkeshi et al., 2021; Xu et al., 2023; Liu et al., 2025). T_s plays a pivotal role in land-atmosphere exchanges. By controlling the partitioning of net radiation into sensible and latent heat fluxes, T_s directly shapes atmospheric boundary layer circulation, with cascading effects on regional climate patterns (Mahanama et al., 2008; Chen et al., 2021a). T_s also drives soil freeze-thaw cycles, which are critical for hydrological processes in cold regions. Permafrost thaw alters subsurface water storage, runoff dynamics and groundwater recharge, with implications for both local and basin-scale hydrology (Zhang et al., 2005; Shati et al., 2018). In addition, it governs the rates of soil microbial activities, nutrient cycling, and organic matter decomposition, with direct implications for carbon dynamics. For instance, T_s modulates microbial respiration, thereby regulating the release of organic carbon into the atmosphere as CO_2 that is central to global carbon cycling (Yang et al., 2011). Given its multifaceted influences on carbon cycling, climate feedbacks and hydrological systems, accurate T_s estimation is indispensable for advancing ecosystem monitoring, refining climate models, and developing effective strategies to mitigate and adapt to climate change.

T_s exhibits high heterogeneity at large spatial scales due to varying driving factors. Solar radiation changes its radiation intensity by adjusting the incident angle and sunshine duration, thus affecting the heating effects on surface soils (Wang and Dickinson, 2013). Additionally, diurnal variations of air temperature cause periodic changes in surface temperature, while the amplitude is often closely related to the local climate and topography. Furthermore, surface covers (e.g., vegetation and snow) significantly impact T_s (Xu et al., 2020; Mortier et al., 2024). Vegetation canopies effectively intercept and scatter solar radiation, while root systems modulate soil moisture distribution, thereby stabilizing deeper soil temperatures (Li et al., 2024). Snow cover, characterized by high albedo, reflects substantial solar radiation and acts as an effective insulator, mitigating cold air penetration and maintaining warmer soil

temperatures during winter months (Myers-Smith et al., 2015). Moreover, thermal conductivity and heat capacity are critical parameters controlling vertical heat transfer in soils. Sandy soils have higher porosity and lower water retention, resulting in lower heat capacity and higher thermal conductivity, thus responding rapidly to temperature changes. In contrast, clay soils have lower porosity and stronger water retention, leading to higher heat capacity and significant thermal stability, characterized by delayed responses to temperature variations (Ochsner et al., 2001; Zhao et al., 2022). Understanding these mechanisms is essential for developing refined vertical T_s distribution models and improving the accuracy of T_s estimation.

Given these complex processes, accurately estimating T_s across different depths is challenging. Quite a few models have been proposed for T_s estimation. These models can be generally classified into physical, statistical or empirical, and machine learning (ML) types (Li et al., 2024; Farhangmehr et al., 2025). Physical models, derived from fundamental heat conduction laws and energy balance equations, provide explicit mechanistic interpretations but suffer from computational complexity and heavy reliance on multi-domain input parameters, which range from soil properties to climatic variables (Gao et al., 2008; Hu et al., 2016; Badache et al., 2016). Statistical or empirical models, such as autoregressive integrated moving average and regression methods (Xing et al., 2018), are usually limited to localized, small-sample applications. Data-driven ML techniques demonstrate a superior ability to capture nonlinear relationships and thus usually can obtain high prediction accuracy. For instance, at site scale, Feng et al. (2019) estimated multi-layer T_s at half-hourly resolutions using Extreme Learning Machine, with a RMSE ranging from 2.26~2.95 K. Li et al., (2022) implemented an attention-aware long short-term memory (LSTM) model for predicting next-day T_s and the model obtained a RMSE of 0.74~2.53 K. At the regional scale, Xu et al. (2023) integrated satellite remote sensing with a deep belief network model to reconstruct continuous T_s profiles (at depths of 5–40 cm) across the Qinghai-Tibetan Plateau (QTP), obtaining $R^2 > 0.836$ and $MAE < 2.152$ °C. Similarly, Farhangmehr et al. (2025) developed a hybrid convolutional neural network-LSTM (CNN-LSTM) architecture for

predicting T_s across North American climatic zones at 0–7 cm depths, with R^2 ranging from 0.93 to 0.99.

90 Although significant advances have been made in estimating T_s , large-scale T_s prediction continues to confront critical challenges, sourcing from environmental complexity and methodological limitations. First, T_s exhibits considerable spatial heterogeneity driven by regional disparities in topography, soil composition, vegetation density, and microclimate (Bayatvarkeshi et al., 2021). These factors create 95 nonstationary relationships between T_s and explanatory variables (e.g., air temperature, soil moisture), necessitating regionally tailored modeling approaches. Second, data scarcity and uneven spatial distribution of site measurements introduce further complexity. Aggregating sparse, unevenly distributed measurements into a single model often leads to overfitting: high accuracy on training data but poor generalization to 100 underrepresented regions or previously unseen data (Li et al., 2024). Ultimately, developing models that reconcile scalability (for large spatial scales) with localized precision (to capture site-specific interactions) remains an unresolved priority, underscoring the persistent challenge of balancing universal applicability with spatially adaptive fidelity in T_s prediction methodology.

105 To address the above challenges, this study proposes a spatially adaptive methodology based on quadtrees. This approach dynamically partitions the study area into grids of varying sizes, with smaller grids in densely observed regions and larger grids in sparsely sampled areas, thereby enabling localized modeling that better captures spatial heterogeneity across complex environmental gradients. In addition, 110 multi-source environmental predictors are integrated, and XGBoost models are applied within each grid cell to capture the nonlinear relationships between T_s and its driving factors. Importantly, we employ a spatial block cross-validation strategy to evaluate the model's generalization ability in unseen regions. Based on this framework, the objectives of this study are to: (1) construct a spatially adaptive modeling system; (2) generate a multi-layer T_s dataset at a daily time-step and one kilometer resolution in 115 China from 2010-2020; and (3) evaluate the dataset through independent validation

with flux tower observations and benchmarking against widely used T_s products. The proposed methodology could directly address the scaling challenges induced by spatial heterogeneity and uneven data distribution. The generated products would provide a 120 robust foundation for high-resolution environmental modeling, precision agriculture and climate impact assessments.

2. Materials and methods

2.1 In-situ T_s observations

125 In this study, in-situ T_s observations was measured at six depths: at the surface (0 m), and at subsurface levels of 0.05, 0.10, 0.15, 0.20, and 0.40 meters. Data were collected through the national weather station network operated by the China Meteorological Administration (CMA), in accordance with standardized measurement protocols. At each site, T_s was recorded every 10 minutes and automatically uploaded 130 to a central server. Daily mean values at each depth were calculated from these high-frequency records. We then assessed data completeness for the period 2010–2020 and excluded stations with more than 20% missing daily records at any depth. After quality control, 2,093 stations were retained for model development.

135 The observation network spans a wide range of climatic zones—from cold and temperate to subtropical and tropical, and includes diverse land-use and ecosystem types, such as forests, grasslands, croplands, and barren lands. However, the spatial distribution of stations is notably uneven. High station density is observed in northeastern China, the central and eastern plains, and the southern hilly regions, whereas station coverage is sparse in the arid and semi-arid regions of northwestern 140 China and on the QTP. The spatial distribution of in-situ observation sites is shown in Figure 1, and details of the dataset partitioning strategy are provided in Section 2.3.3.

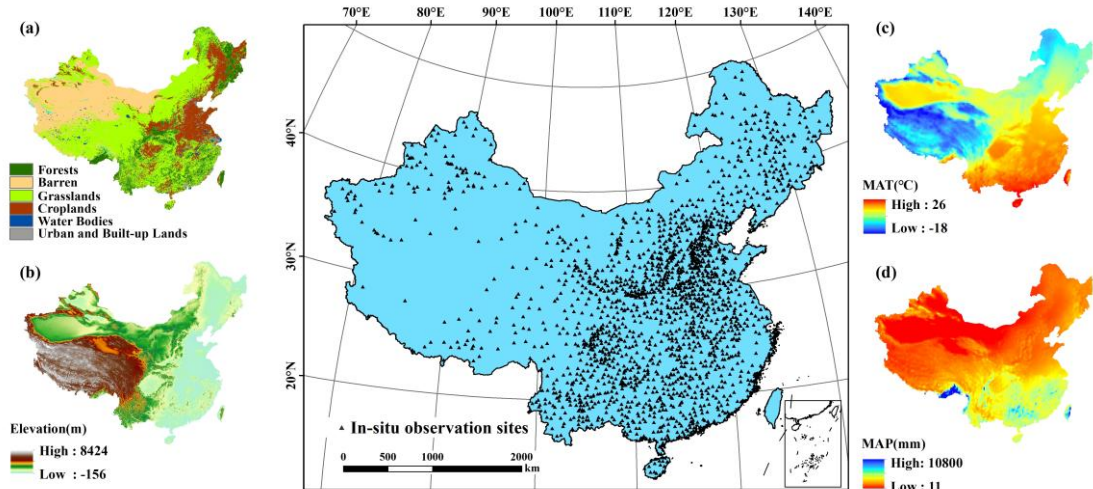


Figure 1. Spatial distribution of in-situ T_s sites at different depths across China and the corresponding environmental variables. This figure presents the spatial distribution of 2,093 in-situ T_s sites across China. The environmental variables corresponding to these sites include (a) land cover types (forests, barren land, grasslands, croplands, water bodies, and urban areas), (b) elevation (ranging from -156 m to 8424 m), (c) mean annual temperature (MAT, ranging from -18°C to 26°C), and (d) mean annual precipitation (MAP, ranging from 11 mm to 10,800 mm).

145

150

2.2 Predictor variables

To construct a robust multi-layer T_s estimation model, we selected a comprehensive suite of predictor variables, integrating remote sensing products, meteorological factors, and auxiliary environmental data. Meteorological variables, especially air temperature and precipitation, have been consistently recognized in previous studies as primary determinants of T_s variability (Bond-Lamberty et al., 2005; Nahvi et al., 2016). Among these, air temperature has been widely regarded as the most influential variable due to its strong linear relationship with T_s (Khosravi et al., 2023).

In addition, both net solar radiation and downward longwave radiation (LWD) were considered. Net solar radiation directly represents the shortwave energy absorbed by the land surface and serves as the primary driver of the daytime surface energy budget, whereas LWD plays a particularly important role under nighttime and winter conditions by regulating surface heat loss through the longwave radiation balance. Together, they jointly control the surface energy balance and directly drive the spatiotemporal dynamics of T_s (Peng et al., 2016).

165

Thermal infrared remote sensing data also exhibit a high correlation with near-

surface T_s . Integrating thermal remote sensing products and energy balance-based models offers an effective means of estimating T_s with high spatial and temporal continuity. This strategy has been validated by numerous studies (Huang et al., 2020; Xu et al., 2023). Surface land cover further modulates T_s by altering surface albedo, 170 regulating evapotranspiration (ET), and influencing energy partitioning processes. Accordingly, the enhanced vegetation index (EVI), derived from satellite observations, was incorporated as a proxy for vegetation density and type (Bright et al., 2017; Li et al., 2024b). To capture the influence of underlying surface characteristics on T_s , topographic variables such as elevation and slope were included, along with soil texture 175 data across various depths. These features collectively reflect the heterogeneous physical and thermal properties of the soil, contributing to spatial variations in heat conduction and storage capacity. A full list of the predictor variables used in the model is summarized in Table 1.

Table 1. Details of the predictor variables for training the model.

Type	Data	Variable	Spatial resolution	Temporal resolution	Reference
Remotely sensed product	MOD09GA	EVI	500 m×500 m	Daily	Huete et al., 2002
	MOD11A1	LST_Day	1 km×1 km	Daily	
	MOD11A1	LST_Night	1 km×1 km	Daily	
Climate data	ERA5-Land	Temperature_2m			
		surface_net_solar_r			
		adiation_sum			Muñoz-
		surface_thermal_ra	9 km×9 km	Daily	Sabater et al.,
		diation_downwards			2021
		_sum			
USGS_STRM		Precipitation			
		Elevation	30 m		
		Slope	30 m		
Supplementary data	Soil Texture	Sand, Silt, Clay			
		Depth:			
		0-5, 5-15, 15-30, 30-60cm	250 m×250 m		Liu et al., 2022
In-situ measurements		Soil temperature			
		at 0, 5, 10, 15, 20, and 40 cm	-	Daily	

180 2.2.1 Remote sensing data

The MOD11A1 LST product, at a daily time-step and a spatial resolution of 1 km, was utilized. It includes both daytime (LST_{day}) and nighttime (LST_{night}) temperatures at 10:30 AM and 10:30 PM, respectively, along with quality assessment information (Wan and Dozier, 1996). To enhance the estimation of daily mean T_s , the average of LST_{day} and LST_{night} values was calculated and used in the analysis.

185 EVI from 2010 to 2020 were selected as predictor of T_s . The MODIS Surface Reflectance Product (MOD09GA), derived from MODIS Level-1B data, provides daily surface reflectance of seven bands at 500 m \times 500 m resolution. The EVI is defined by Huete et al., (2002), and the retrieval equation is as follows:

$$190 EVI = G \times \frac{(\rho_{SR_b1} - \rho_{SR_b2})}{(\rho_{SR_b1} + C_1 \times \rho_{SR_b2} - C_2 \times \rho_{SR_b3} + L)} \quad (1)$$

where $G = 2.5$, $C_1 = 6$, $C_2 = 7.5$, $L = 1$. The remote sensing reflectance variables SR_b1 (620-670nm), SR_b2 (841-876nm) and SR_b3 (459-479 nm) of MOD09GA data represents red, near-infrared and blue bands. The coefficients 2.5 and 1 represent the gain and canopy background, respectively (Huete et al., 2002). The atmospheric influence on the red band is corrected using the blue band and the coefficients 6 and 7.5, respectively.

200 Subsequently, cloud contamination caused partial spatial absences in the daily LST and EVI. To address this issue, we applied a temporal and spatial linear interpolation algorithm, which utilizes time-series data from adjacent days and spatial information from neighboring pixels to fill the current missing values, thereby generating a time-continuous and spatially complete image series. This approach follows the methods described in Chen et al., (2017) and Cao et al., (2018), with modifications to better suit our dataset. Then, the Savitzky-Golay (S-G) filter was used to smooth the interpolated data, resulting in continuous surface temperature and vegetation index data with high 205 temporal and spatial resolution (Kong et al., 2019; Chen et al., 2021b). All data preprocessing, including image filtering and interpolation, was conducted within the Google Earth Engine (GEE) platform.

2.2.2 Climate data

The ERA5-Land is the fifth-generation reanalysis dataset produced by the European Centre for Medium-Range Weather Forecasts (ECMWF). It assimilates multi-source data, including weather station measurements, numerical weather predictions, and satellite observations, into dynamic models to generate reanalysis data (Muñoz-Sabater et al., 2021). It provides high-quality environmental variables related to water and energy fluxes between the land surface and atmosphere, with continuous coverage from 1981 to the present. ERA5-Land offers a spatial resolution of 0.1° (~ 9 km at the equator) and an hourly temporal resolution, making it well-suited for modeling near-surface processes. In this study, we extracted daily mean values of key climate variables, including 2-meter air temperature (Temperature_2m), surface solar radiation and total precipitation from the ERA5-Land Daily dataset. All variables were accessed and processed using the GEE platform.

2.2.3 Auxiliary data

Topographic and soil-related variables were incorporated as auxiliary predictors to improve the accuracy of T_s estimation. Elevation and slope were derived from the Shuttle Radar Topography Mission (SRTM) digital elevation model (Farr et al., 2007), specifically using the Version 3 (SRTM Plus) product with a spatial resolution of 1 arc second (~ 30 m). Soil texture plays a critical role in determining T_s through its influence on thermal conductivity, which is affected by physical properties such as particle size distribution, porosity, bulk density, and moisture retention capacity. In this study, we represented soil texture using the relative proportions of clay (fine), silt (medium), and sand (coarse) particles. To capture vertical variability in soil properties, we employed the China Soil Information Grid dataset developed by Liu et al. (2022), which provides gridded estimates of soil composition at four depth intervals: 0–5 cm, 5–15 cm, 15–30 cm, and 30–60 cm. The dataset offers a spatial resolution of 1 km and is suitable for high-resolution, profile-based soil modeling.

2.3 Methods

The spatial adaptive modeling framework consists of three modules as shown in

Fig. 3. Module I is for data collection and preprocessing, which mainly involves in-situ observations, remote sensing, meteorological and supplementary data. Module II is spatial adaptive modeling, which mainly includes the construction of rotated quadtrees and local modeling based on XGBoost. Finally, module III is the layer-to-layer reconstruction of daily 1km resolution multi-layer (0, 5, 10, 15, 20, and 40 cm) T_s datasets in China from 2010 to 2020.

2.3.1. Feature selection

Multicollinearity among multiple source variables may affect the robustness of the models. Therefore, we rigorously evaluated the multicollinearity among the independent variables using the variance inflation factor (VIF) before modeling to remove highly correlated variables. The VIF is a diagnostic statistic used to quantify the degree of multicollinearity by measuring how much the variance of a regression coefficient is inflated due to correlations with other predictors (Akinwande et al., 2015).

It is calculated as:

$$VIF_i = \frac{1}{1 - R_i^2} \quad (2)$$

where R_i^2 is the coefficient of determination obtained by regressing the i -th predictor against all other predictors. Variables with VIF exceeding 10 are generally considered severely multicollinear and should be removed.

Based on the VIF analysis, we applied the following adjustments to the predictor set. Accordingly, some variables were excluded due to severe multicollinearity or redundancy. Specifically, sand, silt, and clay are compositional variables whose proportions sum to 100%, leading to perfect collinearity. To reduce redundancy, we removed silt while retaining sand and clay. In addition, LWD was found to be highly correlated with net solar radiation at the daily mean scale (Fig. S1) and was therefore excluded from the final modeling.

In contrast, although the daily mean LST (LST_mean) and air temperature also exhibited strong collinearity, with VIF values exceeding 10 (Fig. S2), we decided to retain both. This decision reflects their physical distinctness and complementary

265 information: LST_mean provides higher spatial resolution (1 km), whereas air temperature offers broader meteorological consistency (9 km). Such differences are particularly important in complex ecosystems such as forests, where canopy structure and biological processes substantially influence thermal dynamics (Liu et al., 2025).

2.3.2. Spatial adaptive partition of site measurements

270 A quadtree is a hierarchical spatial data structure that recursively subdivides a two-dimensional space into four quadrants, enabling efficient spatial indexing and localized data organization. In this study, we adopted a bottom-up, rotated quadtree-based spatial partitioning strategy that adaptively generates finer grids in regions with dense samples and coarser grids in sparse regions. Compared to global modeling or static grid 275 partitioning, this adaptive approach offers improved regional modeling fidelity while significantly enhancing computational efficiency. The procedure consists of the following steps:

(1) Initialization of Minimum Units

280 The entire spatial domain was first divided into uniform, minimum-sized units (leaf nodes), each representing a fundamental spatial element. These units may contain zero or more in-situ observations. This initial step provides the base resolution for subsequent hierarchical construction. The structure and principle of quadtree spatial indexing are illustrated in Fig. S3.

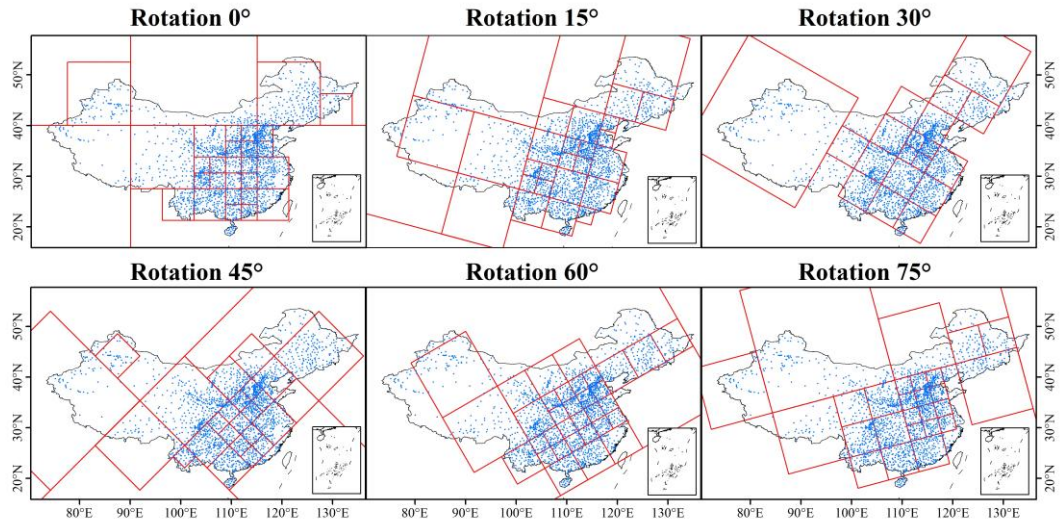
(2) Hierarchical Merging

285 Starting from the leaf nodes, groups of four adjacent quadrants were recursively merged into parent nodes if each contained fewer than 30 observation sites (threshold selection detailed in Fig. S4). The merging process continued upward until no further groups met the threshold. This approach ensures that each node has sufficient sample size while achieving spatially adaptive partitioning across the study area. Each 290 subregion is then assigned a localized T_s prediction model.

(3) Rotation at different angles

To reduce potential edge effects introduced by static grid boundaries, we implemented a rotated quadtree partitioning strategy. The quadtree structure was rotated

at six angles (0° , 15° , 30° , 45° , 60° , and 75°), producing distinct sets of spatial partitions for each orientation (Fig. 2). Independent models were trained for each rotated configuration, and the final T_s estimates were obtained by averaging the outputs from all six models. This rotation-based ensemble method improves spatial smoothness and minimizes discontinuities at partition boundaries.



300 **Figure 2.** multi-angle adaptive quadtree partitioning of site observations (0° , 15° , 30° , 45° , 60° , 75°)

2.3.3. Machine learning algorithm

We adopted the XGBoost (Extreme Gradient Boosting) algorithm as the core regression model for T_s estimation due to its strong predictive performance, computational efficiency, and scalability across large environmental datasets. XGBoost constructs an ensemble of regression trees in a stage-wise boosting process, where each successive tree is trained to minimize the residuals of the previous iteration, thereby producing a robust and optimized model (Chen and Guestrin, 2016). One of the key strengths of XGBoost is its ability to handle heterogeneous and high-dimensional predictor sets, which are common in geoscience applications involving complex terrain, land cover variability, and climatic gradients. Recent studies have demonstrated its effectiveness in similar domains, including land surface temperature reconstruction (Li et al., 2024), multi-layer soil moisture estimation (Karthikeyan and Mishra, 2021), drought event attribution (Wang et al., 2025a), and crop yield prediction (Li et al.,

315 2023b). Given these proven strengths and the spatially nonstationary characteristics of T_s in our study area, XGBoost was selected to train localized prediction models within spatial subregions.

320 To rigorously account for the strong spatial autocorrelation of T_s and avoid potential data leakage between training and testing subsets, we employed a spatial block cross-validation scheme rather than random splitting. Specifically, within each rotated quadtree grid, observation sites were grouped into spatial blocks based on their geographic coordinates: station latitude and longitude were each divided by 1° and floored to integer values, and stations sharing the same index were assigned to the same block. This ensured that samples within the same spatial block were not simultaneously 325 assigned to both the training and testing subsets, thereby avoiding data leakage due to spatial autocorrelation and enabling a more reliable evaluation of the model's generalization capability.

330 Within each spatial grid, the data were partitioned into training (90%) and testing (10%) subsets at the block level. The training subset was further subjected to 10-fold spatial block cross-validation using GridSearchCV to optimize three key hyperparameters: the number of trees (n_estimators), maximum tree depth (max_depth), and learning rate (learning_rate). Detailed parameter settings are provided in Appendix Table S1. The hyperparameter set that yielded the lowest average validation error across the ten folds was selected as optimal. The final model was retrained on the full training 335 set with the optimized parameters and evaluated on the held-out testing set to assess generalization.

340 A layer-wise prediction strategy was adopted to estimate T_s along the soil profile. For the surface layer (0 cm), predictors included air temperature and daily mean LST. For subsurface layers, these two variables were replaced by the T_s estimate from the immediately preceding layer, enabling the model to capture vertical heat conduction processes and thereby improving the continuity and physical consistency of layer-wise T_s estimation.

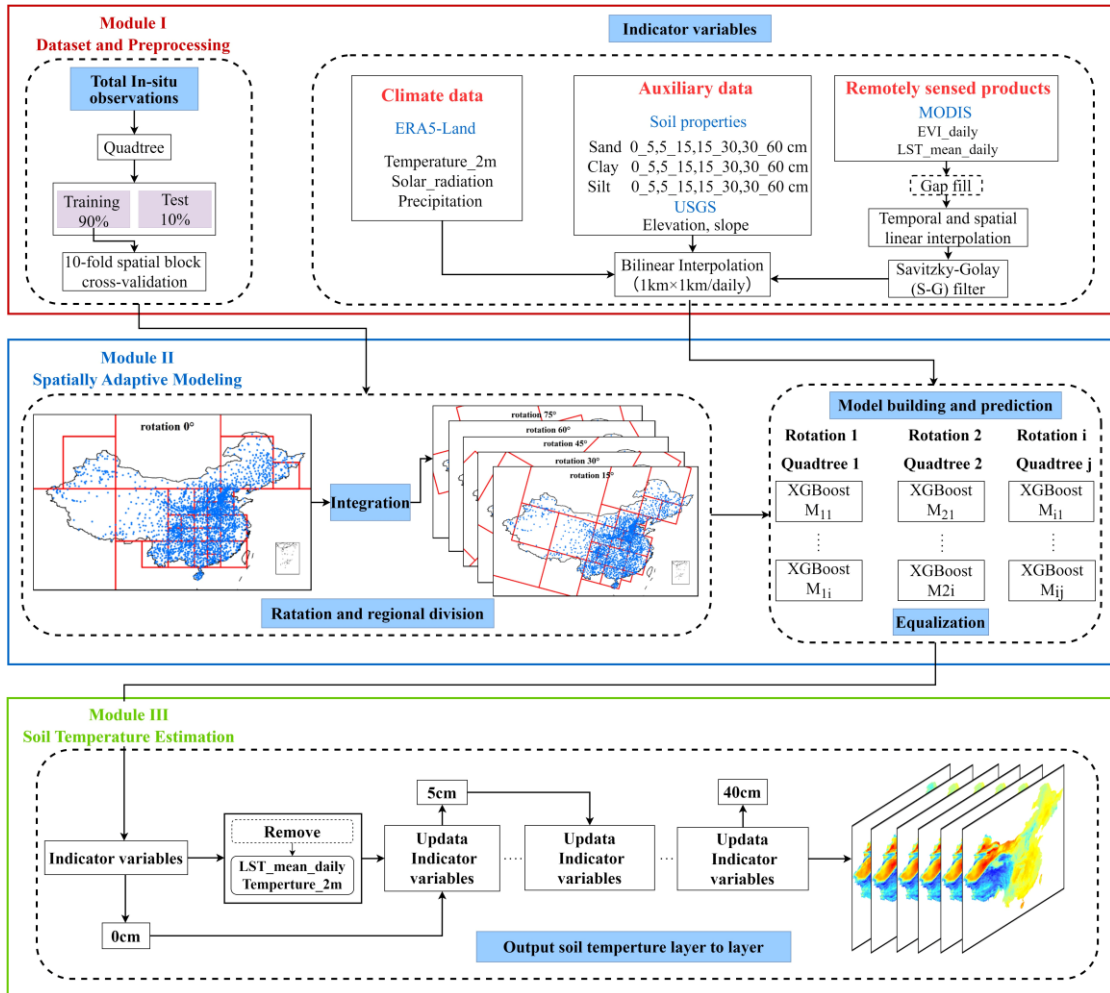


Figure 3. Workflow of the proposed method to obtain multi-layer T_s over the China.

345 2.3.4. Model evaluation metrics

The modeling performance and quality of the predicted T_s were evaluated in terms of RMSE, Mean Absolute Error (MAE), R^2 , and Bias. RMSE and MAE were used to assess the ability to estimate volatility and fluctuation amplitude, respectively. R^2 represented the percentage of variance explained by the ML models. Bias was used to determine whether the estimations were overestimated or underestimated. These metrics were computed as follows:

$$RMSE = \sqrt{\frac{\sum_{i=1}^N [(x_i - \bar{X}) - (y_i - \bar{Y})]^2}{N}} \quad (3)$$

$$MAE = \frac{\sum_{i=1}^N |x_i - y_i|}{2} \quad (4)$$

$$Bias = \frac{1}{N} \sum_{i=1}^N (x_i - y_i) \quad (5)$$

$$R^2 = 1 - \frac{\sum_{i=1}^N (y_i - \bar{x}_i)^2}{N \sum_{i=1}^N (y_i - \bar{Y})^2} \quad (6)$$

where y_i and x_i denoted the in-situ T_s and estimated T_s for all the stations and periods,
 360 respectively. \bar{Y} and \bar{X} represented the mean values of the in-situ T_s and estimated T_s ,
 respectively.

3. Results

3.1 Model performance across sites

365 Figure 4 illustrates the accuracy performance of all models constructed at various
 depths, utilizing different grid configurations and rotation angles, for both the training
 and test sets. The grouped box plots demonstrate that the R^2 values for the training and
 test sets at different depths range from 0.82 to 0.98, and the RMSE values vary from
 0.6 to 2.8 K. Both the training and test sets exhibit high accuracy with no evident signs
 370 of overfitting. A depth-wise comparison shows that model performance at 0 cm and 40
 cm is marginally lower than at other depths.

375 Furthermore, to enhance the independence of the evaluation, we validated the final
 dataset against daily T_s observations from 18 flux tower sites of the ChinaFLUX
 network. For consistency, we retained measurements only at depths of 0, 5, 10, 15, 20,
 and 40 cm. Metadata for these sites is provided in Table S2, and the corresponding
 validation results are presented in Figure 5. The evaluation shows that our dataset
 achieves high accuracy at these independent sites ($R^2 = 0.85\text{--}0.90$; RMSE = 3.3–4.2 K),
 further demonstrating the robustness of our approach. Taken together, the validation
 results from both spatial block cross-validation and flux tower observations confirm
 380 that the spatially adaptive model we developed exhibits reliable accuracy and strong
 spatial generalization capability.

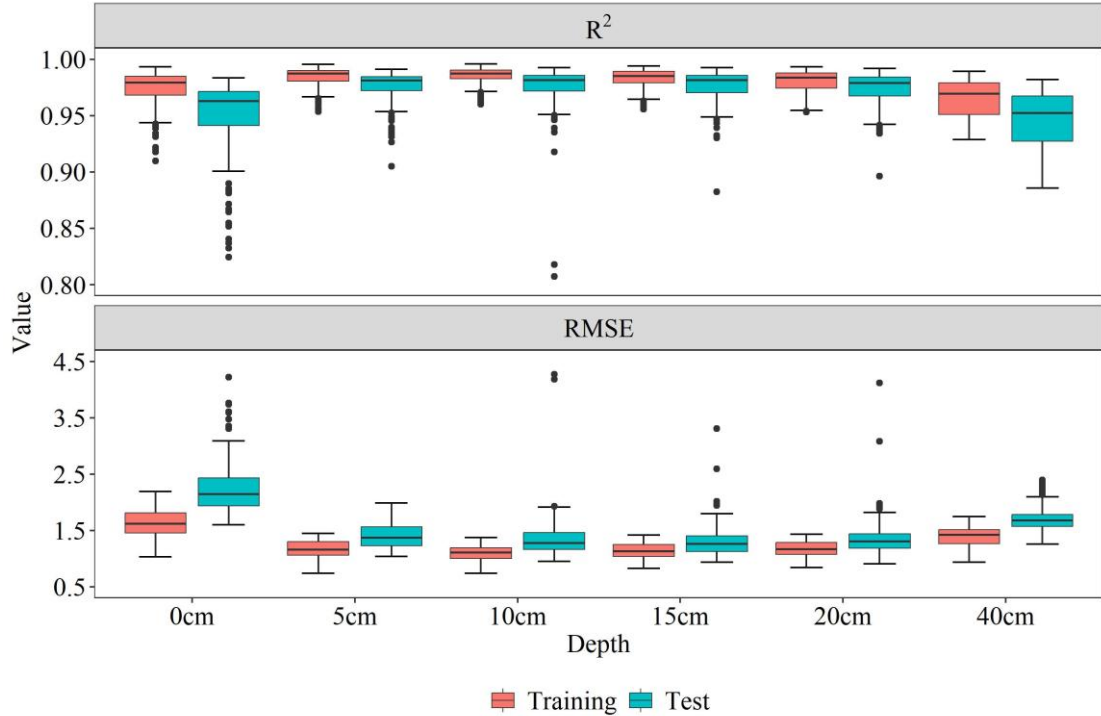
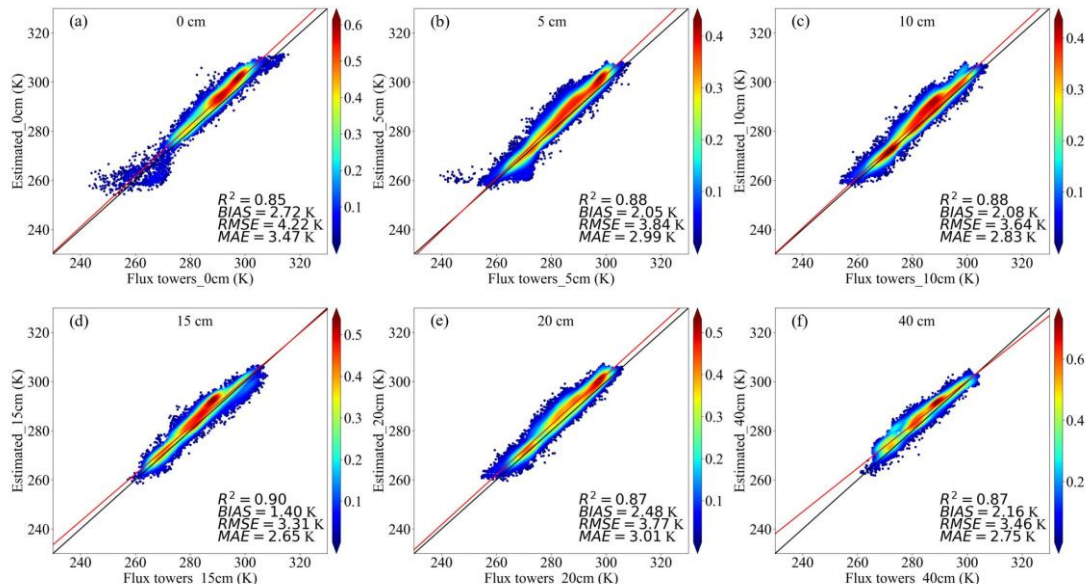


Figure 4. Model performance for training and test sets across different depths.



385

Figure 5. Density scatter plots comparing estimated daily T_s with flux tower observations at different depths

3.2 Model performance at individual sites

To evaluate spatial prediction accuracy in the spatial-scale evaluation, R^2 and RMSE were calculated at each station. Model performance was assessed across all soil depths at the station level. Spatial results show that station-level R^2 values range from 0.70 to 1.00, and RMSE values range from 0 to 3 K, indicating acceptable prediction

accuracy across all soil layers. As illustrated in Figures 6 and 7, most stations achieve R² values above 0.90. Regions with higher prediction accuracy are mainly located in the northwest, northeast, and central areas, whereas larger errors are concentrated in the Yunnan–Guizhou Plateau (YGP) and the sparsely monitored QTP. The histogram in Fig. 7 further shows that RMSE values for most depths fall between 0.5 and 2.0 K, indicating generally good predictive performance. Notably, prediction errors were highest at the surface layer (0 cm), decreased with depth, but slightly increased again at 40 cm, where performance was weaker than at 5–20 cm.

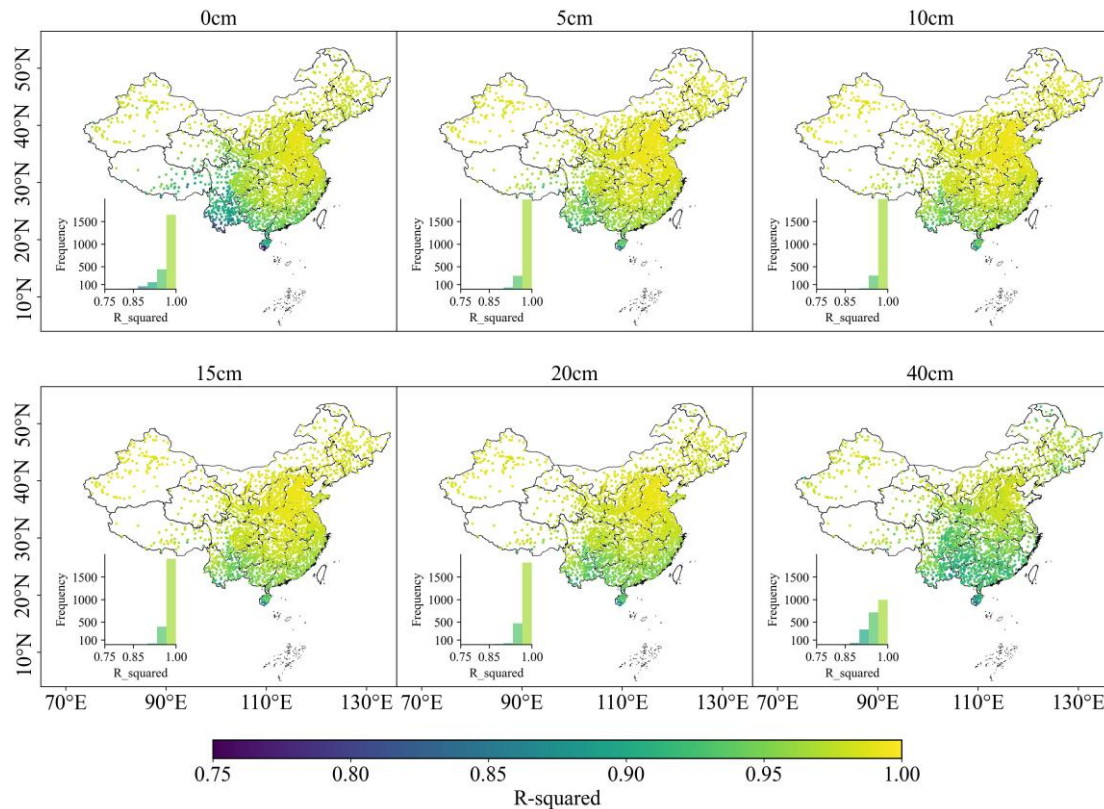


Figure 6. Goodness of R² across China estimated during the model testing phase. Performance metrics are calculated between predicted T_s and in-situ T_s data sets.

405

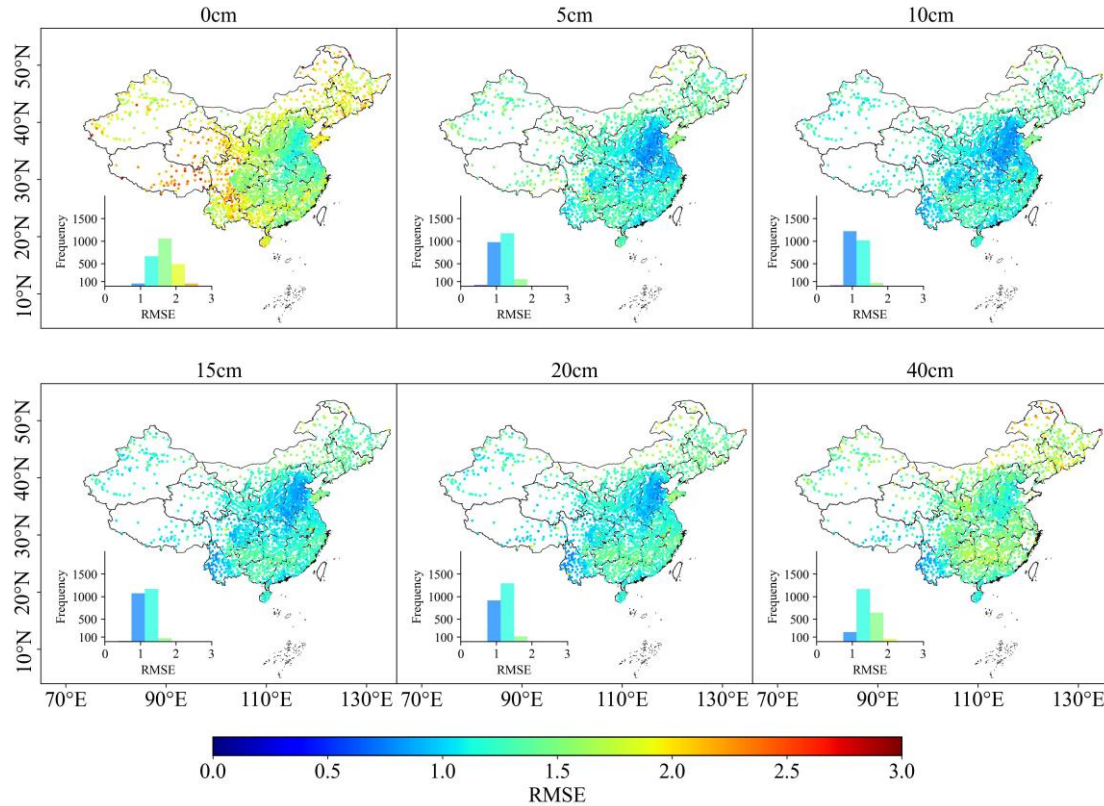


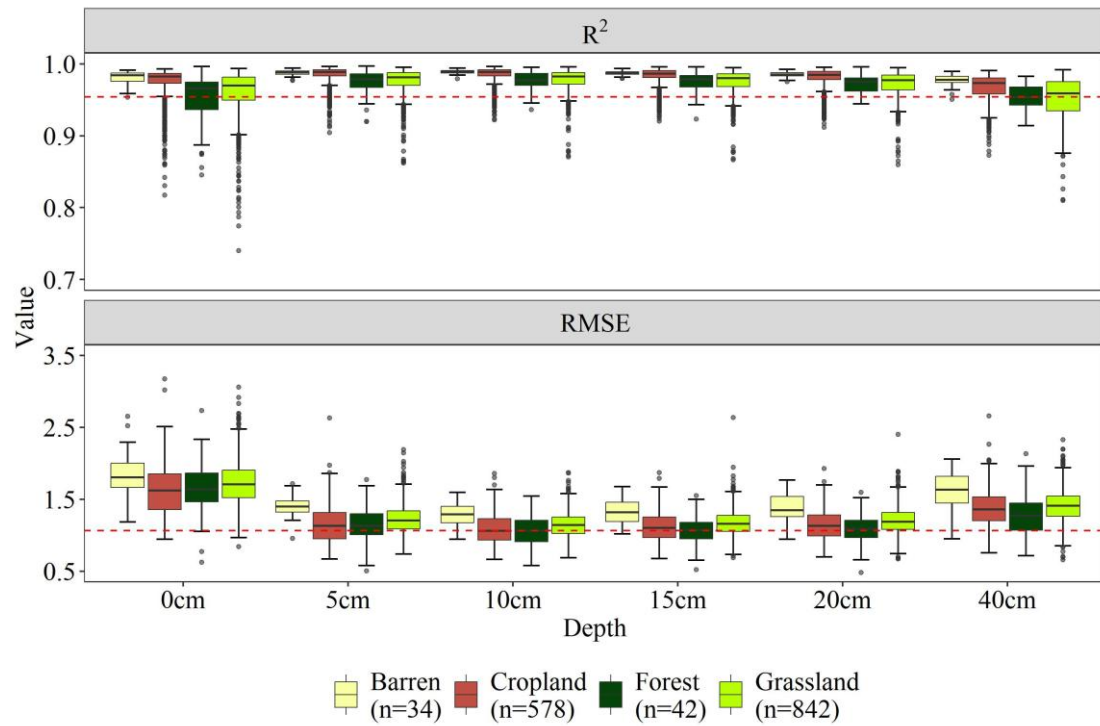
Figure 7. Goodness of RMSE across China estimated during the model testing phase. Performance metrics are calculated between predicted T_s and in-situ T_s data sets.

3.3 Evaluation across land cover types and seasons

410 Figure 8 shows grouped box plots of the prediction performance of T_s across different land cover types (barren land, cropland, forest, and grassland) at six depths (0, 5, 10, 15, 20, and 40 cm). The evaluation metrics include R^2 and RMSE. The median 415 R^2 values across land cover types and depths range from 0.96 to 0.98, consistently exceeding 0.96 (red dashed line), indicating overall high prediction accuracy. Among land cover types, barren land exhibits the highest R^2 values, followed by cropland, while forest and grassland show slightly lower performance. The median RMSE values generally range from 1.1 to 1.8 K. Barren land shows higher RMSE compared with other land cover types, whereas cropland, forest, and grassland maintain lower and more stable RMSE. Across depths, RMSE is highest at the surface layer (0 cm), 420 decreases steadily with increasing depth, and shows a slight increase at 40 cm.

Furthermore, seasonal variations in prediction accuracy are shown in Fig. 9. The median R^2 values across depths range from 0.6 to 0.98, with higher values in spring (green) and autumn (pink) and lower values in summer (orange) and winter (blue),

particularly at 20–40 cm depth. The median RMSE values range from approximately 425 1.0 to 2.0 K, being lower in spring and autumn and higher in summer and winter, with the largest median error observed at 40 cm depth in winter. With increasing soil depth, the median errors decrease from the surface (0 cm) to 5–10 cm, and then gradually accumulate from 15 to 40 cm.



430 **Figure 8.** Evaluation of predicted T_s at different depths (i.e., 0, 5, 10, 15, 20, 40cm) across various land use types (i.e., Forest, Grassland, Cropland, Barren)

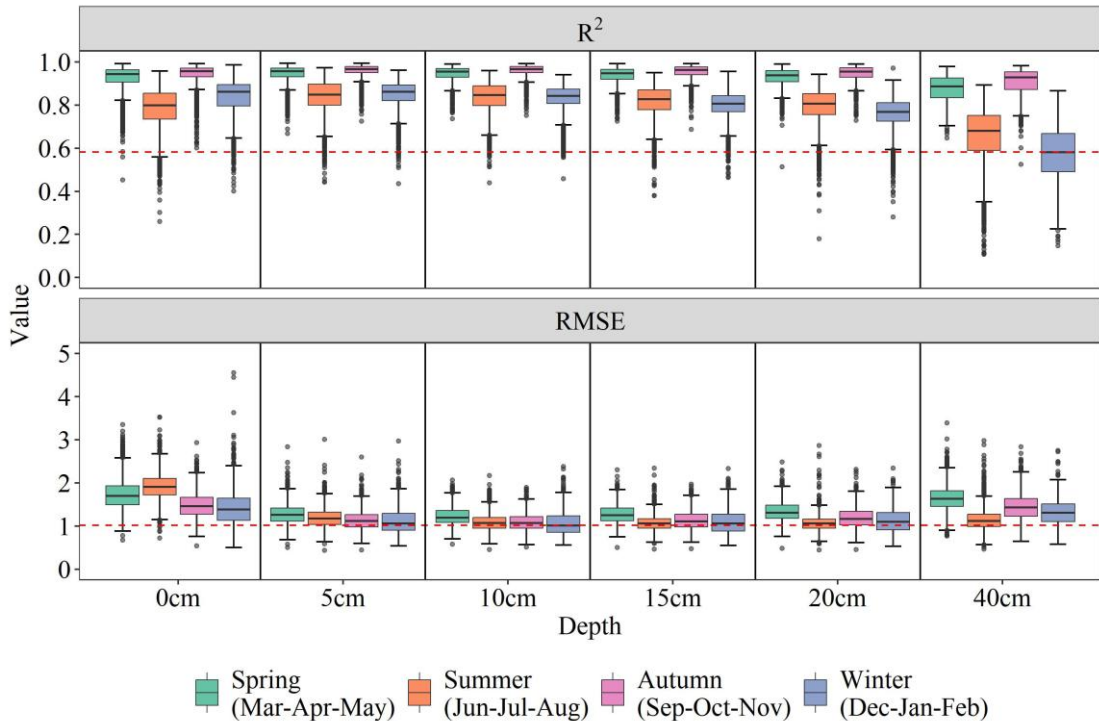


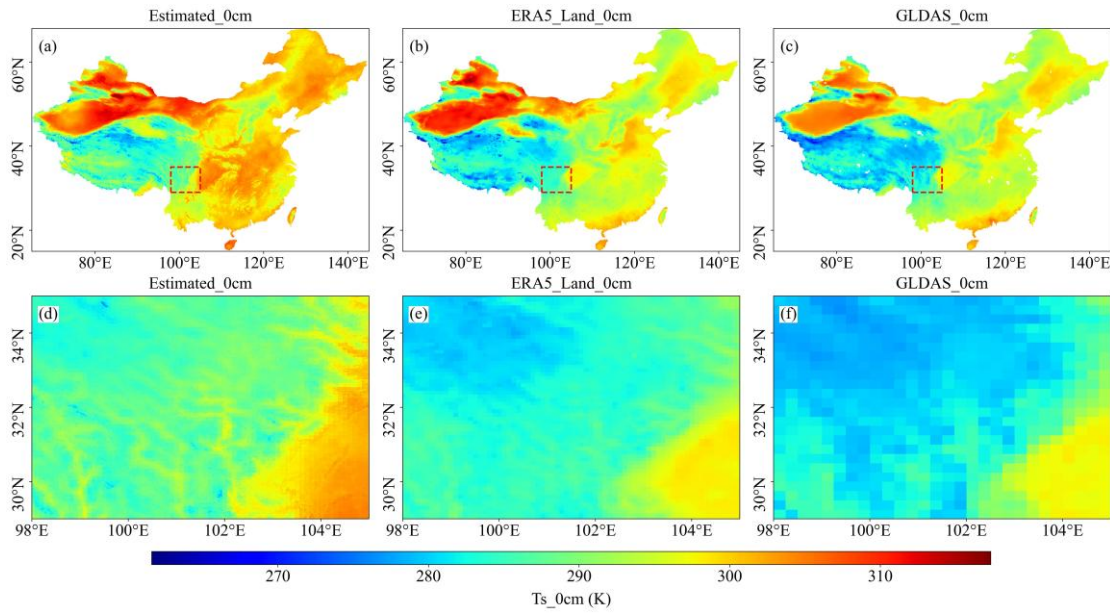
Figure 9. Evaluation of the predicted T_s in different depth (i.e. 0, 5, 10, 15, 20, 40 cm) at sites with four seasons (i.e., spring, summer, autumn, winter). Winter is defined as December, January, and February; spring as March, April, and May; summer as June, July, and August; and autumn as September, October, and November.

3.4 Comparison with other products

Figure 10 presents a comparative analysis of different T_s products at the surface (0 cm depth), evaluating the spatial characteristics of the model-generated T_s against the ERA5-Land and GLDAS 2.1 products across both national-scale regions (Fig. 10a–c) and zoomed-in local areas (Fig. 10d–f). Compared to the GLDAS 2.1 product (Fig. 11c and 11f), the model generated T_s exhibits significantly finer spatial resolution and a superior ability to capture localized spatial heterogeneity. The GLDAS 2.1 product, characterized by a coarser resolution, inadequately represents local features and exhibits notable limitations, especially in specific regions (Fig. 10f). Conversely, the spatial distribution of our T_s data closely matches that of the ERA5-Land product (Fig. 10b and 10e). Nevertheless, the ERA5-Land product may be constrained by its input resolution, whereas our adaptive modeling approach achieves greater precision in representing fine-scale spatial variability.

Scatter density plots in Fig. S5 further indicate that our estimated T_s achieves significantly higher site-level accuracy compared to ERA5-Land and GLDAS 2.1.

Specifically, the R^2 values between in-situ observations and our estimations at depths of 0, 10, and 40 cm range from 0.94 to 0.97, compared to 0.83–0.89 for ERA5-Land and 0.83–0.87 for GLDAS 2.1. These results underscore the reliability and enhanced accuracy of our T_s estimation product at both spatial and site scales, effectively overcoming the limitations associated with GLDAS 2.1 and ERA5-Land products. These findings highlight the strong potential of the model to accurately capture the spatial distribution of T_s and enhance regional-scale T_s modeling.



460

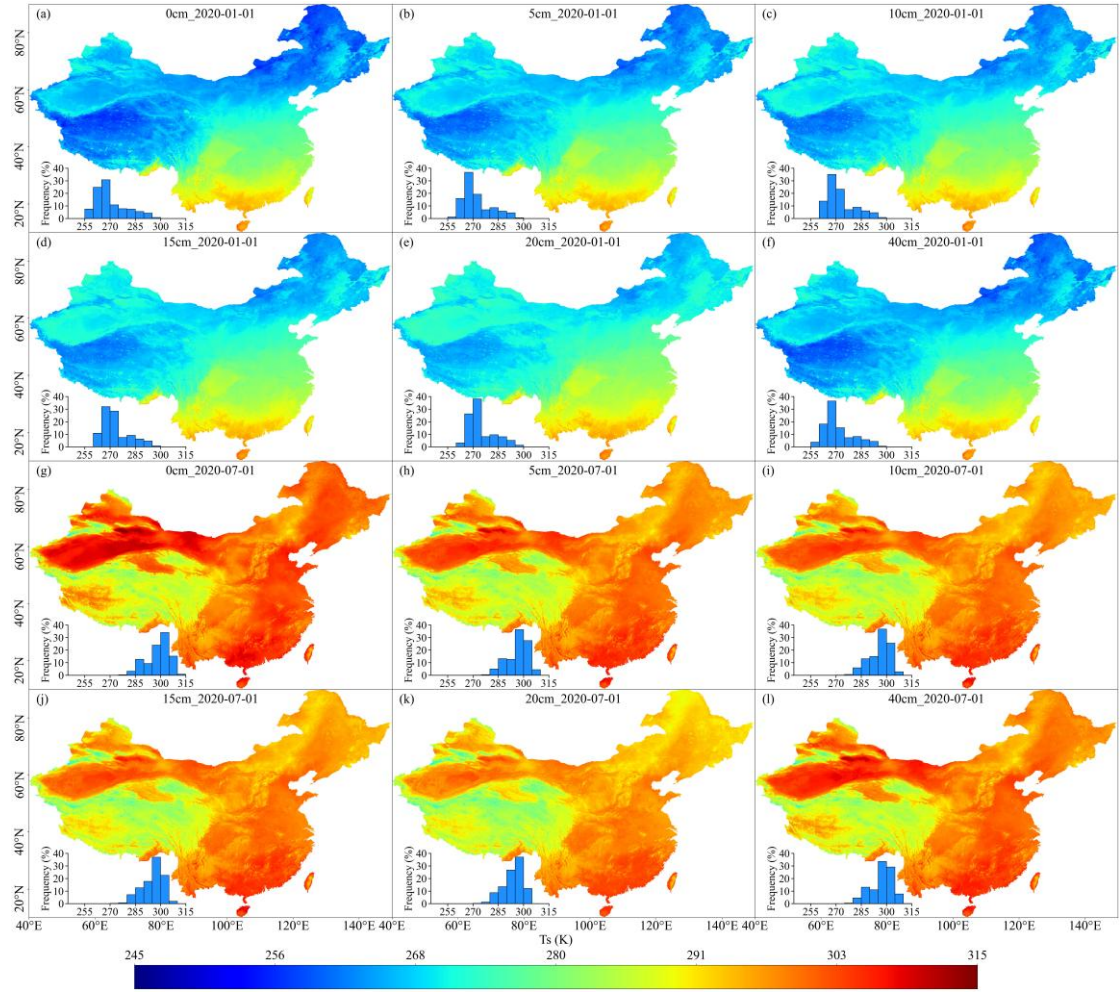
Figure 10. Comparison of different T_s products (e.g., 0 cm)

3.5 Spatial and temporal patterns of T_s at varied depths across China

To examine seasonal and vertical variations in the spatial distribution of T_s , we selected two contrasting dates: January 1, 2020 (winter) and July 1, 2020 (summer). Figure 11 a–f illustrates the spatial distribution and corresponding histograms of T_s at different depths (0 cm, 5 cm, 10 cm, 15 cm, 20 cm, 40 cm) across China on January 1, 2020. The results show that T_s in northern China (particularly in the northeast, northwest, and the QTP) is generally lower in January, exhibiting distinct cold zones. In contrast, southern areas exhibit higher T_s values, forming a gradual north-to-south temperature gradient. Moreover, deeper soil layers (e.g., 40 cm) exhibit higher temperatures than surface layers (0 cm), especially in northeastern China and the QTP, reflecting the insulating effect of deeper soils during winter.

Figure 11a1–f1 illustrates the spatial distribution and histograms of T_s on July 1,

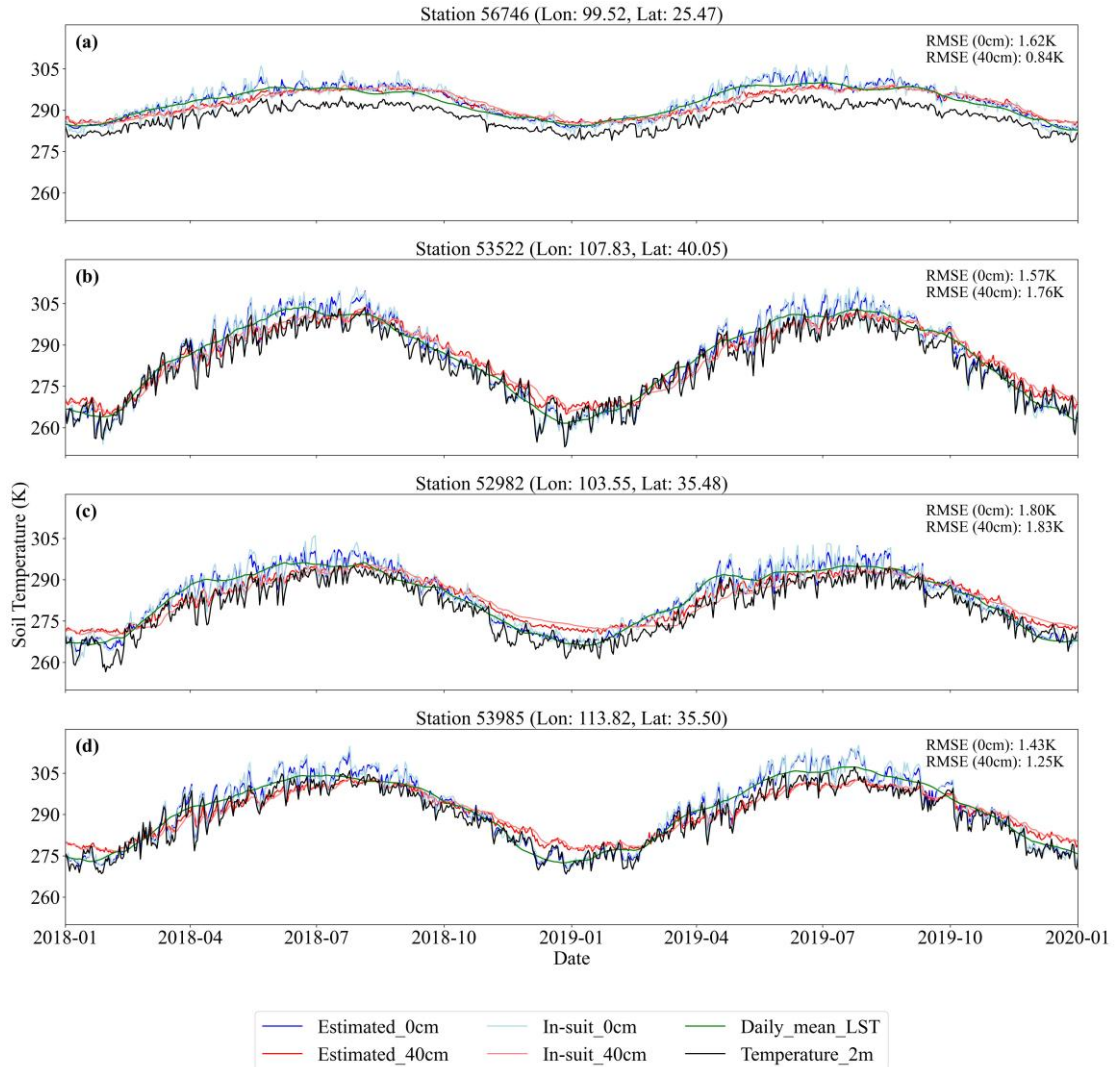
2020. Compared to January, a significant increase in T_s is observed across China in July,
475 with widespread high-temperature zones in the eastern and southern regions. The
increase is particularly pronounced in northern areas, while changes in the south are
relatively moderate. In contrast to winter conditions, T_s decreases with increasing soil
depth during summer, with surface temperatures (0 cm) exceeding those at 40 cm,
indicating the downward heat conduction from the surface. Overall, Comparative
480 analysis of Fig. 11a–f and Fig. 11a1–f1 elucidates both seasonal variation and vertical
patterns of T_s : deeper layers (5–40 cm) are warmer than the surface (0 cm) during winter,
whereas the surface is warmer in summer. The histogram further illustrates the variation
in T_s distribution across different depths. The results indicate that temperature
fluctuations in deeper soil layers are significantly smaller than those near the surface,
485 reflecting greater thermal stability in the subsurface. These patterns reflect the
combined influences of geographic location, topography, and climatic conditions on T_s
spatial distribution and vertical dynamics, offering valuable insights into soil thermal
behavior.



490 **Figure 11.** Spatial patterns and histograms of Estimated T_s at different depths (0, 5,
 10, 15, 20, and 40 cm)

To further assess the temporal performance of T_s estimation, Fig. 12 presents the time series of estimated T_s alongside in-situ measurements at four randomly selected stations (e.g., Station 56746, 99.53°E, 25.45°N) from January 2018 to January 2020. The figure displays T_s at two depths (0 cm and 40 cm), including estimated T_s (Estimated_0cm, Estimated_40cm), in-situ T_s (In-situ_0cm, In-situ_40cm), daily mean land surface temperature (Daily_mean_LST), and 2-meter air temperature (Temperature_2m). The air temperature shows distinct seasonal cycles, while T_s exhibits smoother temporal variations. In general, T_s reaches its peak during summer and its minimum in winter, though its temporal dynamics vary with soil depth. Specifically, T_s at 0 cm responds rapidly to air temperature changes and exhibits larger amplitude variations, while T_s at 40 cm shows slower responses and a noticeable lag,

reflecting the damping effect of vertical heat conduction. Site-level accuracy was evaluated using RMSE, which ranged from 0.84 K to 1.80 K across both depths, indicating strong agreement between predicted and observed values. Overall, the time series analysis confirms the robustness and reliability of the model in estimating T_s across varying depths, offering valuable insights into regional soil thermal dynamics.



510 **Figure 12.** Time series of the Estimated_0cm, Estimated_40cm, Daily_mean_LST, and Temperature_2m at four sites from different regions between 2018-2019.

4. Discussion

515 4.1 The advantages of the spatially adaptive model

Previous studies have explored various approaches for constructing T_s datasets. For instance, Wang et al., (2023) created a daily multi-layer T_s dataset for China (1980-

2010) at 0.25° resolution, employing interpolation techniques including the thin-plain 520 spline and the angular distance weight interpolation methods with over 2,000 in-situ observations. A persistent challenge in building national-scale T_s datasets, however, lies in the highly uneven spatial distribution of observation stations—densely clustered in eastern lowlands while remaining sparse in western and high-altitude regions. Global modeling approaches, which train a single unified function across the entire domain, are inherently limited in capturing the nonlinear and non-stationary relationships 525 between T_s and its predictors in such heterogeneous landscapes. Specifically, in sparsely sampled regions, global models lack sufficient data to learn effectively, resulting in low prediction accuracy. In contrast, in densely sampled areas, the model tends to overfit, and the training process becomes disproportionately influenced by those regions. This imbalance introduces systematic biases and limits model generalizability.

530 Reanalysis datasets, which synergize data assimilation systems with numerical weather prediction and land surface modeling frameworks, provide valuable representations of land-atmosphere interactions and subsurface heat transfer processes. These products are particularly advantageous for large-scale climate simulations and long-term environmental assessments. Yang and Zhang (2018) assessed the T_s accuracy 535 of four reanalysis datasets (ERA-Interim/Land, MERRA-2, CFSR, and GLDAS-2.0) in China using in-situ monthly mean T_s observations. The results showed that all reanalysis datasets consistently underestimated T_s across the country. More recently, the ERA5-Land and GLDAS 2.1 T_s dataset offers high temporal resolution (hourly/3-hour), but it is limited by a spatial resolution of 0.1 or 0.25 degrees. Beyond reanalysis datasets, 540 some efforts have focused on constructing empirical T_s products using ML approaches. For example, the Global Soil Bioclimatic Variables dataset (Lembrechts et al., 2022), derived from Random Forest modeling with 8,519 global sensors, provides only long-term climatological means, rather than high-resolution daily estimates.

545 In contrast, the methodological framework proposed in this study addresses both accuracy and resolution limitations. The spatially adaptive modeling strategy offers significant advantages over traditional interpolation and globally trained ML models.

Its core strength lies in localized modeling, which accounts for regional variability in topography, soil properties, and climate conditions. As shown in Fig. S6, the rotated quadtree strategy partitions space at six orientations (0°–75°), enabling a more nuanced representation of spatial heterogeneity. By averaging predictions across these rotated configurations, the method reduces boundary artifacts often associated with static grids, resulting in smoother and more continuous spatial outputs. Moreover, the fine spatial resolution (1 km) enables the model to resolve localized thermal patterns that are critical for understanding vegetation dynamics and soil biogeochemistry. We also assessed the contribution of satellite-derived LST to model performance. As shown in Figs. S7 and S8, incorporating LST as an input variable, relative to using only air temperature, significantly enhances overall modeling accuracy and improves performance across sites with different land cover types, with the most pronounced improvements observed in barren land areas. This highlights the importance of multi-source data fusion in boosting the performance of spatially adaptive models under data-scarce conditions. In summary, our spatially adaptive local modeling approach offers a more robust and scalable solution for large-scale T_s estimation under heterogeneous station distributions and complex environmental conditions.

4.2 Potential applications of the T_s product

The high-resolution, multi-layer T_s datasets generated using the spatially adaptive estimation method fill a significant data gap in China, where comprehensive T_s profile records are scarce. As a key biophysical variable, T_s provides crucial insights into soil–atmosphere interactions that are not captured by air temperature alone. In agricultural systems, T_s governs fundamental processes throughout the crop life cycle—from sowing and germination to growth and yield formation (Rahman et al., 2019). Multi-layer T_s data can optimize accumulated temperature models, enhancing the precision of sowing decisions and supporting sustainable field management. Additionally, T_s influences nutrient decomposition and water movement within soil profiles (Jebamalar et al., 2012), directly impacting soil fertility, moisture retention, and thus, the overall efficiency of agroecosystems.

Beyond agricultural applications, T_s is increasingly recognized as a critical variable for assessing ecosystem responses to climate extremes. For instance, Fan et al., (2024) proposed the Soil Composite Drought Heatwave index to evaluate the severity of concurrent drought and heatwave events. However, their findings show that existing 580 reanalysis datasets often underestimate these events compared to observational records, highlighting the need for more accurate, high-resolution T_s data. In the context of intensifying global warming and extreme climate events, access to reliable T_s datasets is essential for improving the monitoring and prediction of environmental stressors. These advancements are not only vital for understanding terrestrial ecosystem 585 dynamics but also for strengthening climate resilience at both regional and national scales.

Moreover, T_s plays a pivotal role in ecological and hydrological modeling, offering a more direct representation of surface processes than air temperature. It serves as a sensitive indicator of biogeochemical cycles and phenological changes (Lembrechts et 590 al., 2022). For example, Liu et al., (2024) demonstrated that T_s is a dominant driver of spring phenology in Chinese forests, making it a valuable input for climate–vegetation interaction models. In cold regions, T_s governs soil freeze–thaw cycles, which are critical for hydrological processes such as runoff generation, groundwater recharge, and permafrost monitoring (Smith et al., 2022; Xu et al., 2022). Furthermore, T_s is a key 595 driver of soil respiration, influencing CO₂ fluxes and terrestrial carbon cycling (Lloyd and Taylor, 1994; Hursh et al., 2017). As such, the development of high-resolution T_s products enables more accurate simulation of ecosystem carbon dynamics and regional carbon budgeting, thereby advancing our understanding of climate feedback mechanisms.

600 4.3 Limitations and future perspective

Despite the strong performance of our spatially adaptive T_s estimation framework, several limitations warrant acknowledgment. As shown in Figures 6 and 7, model validation at station level reveals spatial heterogeneity in prediction accuracy, with relatively lower performance observed in the YGP and the QTP regions. On the one

605 hand, as evidenced by Figure 10, our multi-source modeling framework captures T_s variations across different elevations and geomorphic conditions more effectively than existing datasets. However, the QTP and YGP are characterized by complex terrain and high altitudes, coupled with rapidly changing climatic conditions, which significantly complicate T_s estimation. These findings align with previous studies showing that high 610 elevations intensify the disconnect between air temperature and LST, thereby increasing the uncertainty in thermal modeling (Mo et al., 2025).

MODIS LST serves as a critical input to our modeling framework. However, as an optical remote sensing product, it is highly susceptible to cloud contamination, often resulting in data gaps. Despite the use of spatiotemporal interpolation and SG filtering, 615 residual uncertainties persist in the reconstructed LST data. Future improvements in T_s reconstruction can be pursued along two main directions. First, more physically grounded LST reconstruction methods can be adopted, such as incorporating surface energy balance models and diurnal temperature cycle models (Hong et al., 2022; Firozjaei et al., 2024; Wang et al., 2024). These methods apply energy conservation 620 principles to estimate T_s during periods of missing or unreliable observations, thereby providing more realistic estimates of land surface thermal conditions during periods of cloud cover. Second, integrating higher temporal resolution remote sensing observations may help overcome the limitations of MODIS. For instance, passive 625 microwave satellite data provide all-weather observations and are less sensitive to cloud interference (Duan et al., 2017; Wu et al., 2022). In addition, next-generation geostationary satellites such as Himawari-8 offer observations at 10-minute intervals, substantially enhancing the temporal continuity and quality of surface temperature 630 estimates (Yamamoto et al., 2022; You et al., 2024). These enhancements are expected to significantly improve the accuracy and temporal continuity of soil temperature monitoring.

Our results (Figures 8 and 9) show that model accuracy varies across different soil depths, with additional influences from season and land use. Accuracy is relatively lower at the surface (0 cm), improves at intermediate depths (5–10 cm), and then

declines again at greater depths (20–40 cm). This depth-dependent pattern can be
635 explained by the physical characteristics of soil temperature. Surface soil temperature
is highly sensitive to short-term meteorological fluctuations such as radiation,
precipitation, and evapotranspiration, leading to greater spatiotemporal variability and
larger prediction errors. In contrast, intermediate soil layers benefit from the buffering
640 effects of thermal diffusion and soil heat capacity, which dampen high-frequency
fluctuations and stabilize the relationship between predictors and T_s , thereby improving
performance at these depths. At greater depths, however, surface-level errors propagate
downward through the cascading framework, resulting in reduced accuracy —
particularly during summer and winter.

Seasonal changes and variations in land cover further contribute to differences in
645 estimation accuracy. As shown in Figures 8 and 9, the model exhibits higher accuracy
in spring and autumn, whereas its performance tends to decline during summer and
winter. During summer, dense vegetation growth and canopy closure reduce the
influence of surface–atmosphere energy exchanges on T_s , weakening the correlation
between canopy temperature and subsurface T_s (Kropp et al., 2020; Cui et al., 2022). In
650 winter, snow cover introduces a suite of confounding effects: high surface albedo
reduces net radiation (Loranty et al., 2014; Li et al., 2018), while snow acts as an
insulator, limiting the soil's response to cold air incursions (Zhang, 2005; Myers-Smith
et al., 2015). Additionally, low temperatures lead to soil water freezing, which alters the
soil's thermal conductivity and heat storage capacity. These factors, together with
655 frequent freeze–thaw cycles, introduce complex nonlinear dynamics in T_s that increase
modeling uncertainty (Li et al., 2023a; Imanian et al., 2024). While our multi-source
adaptive modeling framework performs well across depths, it does not explicitly
account for the physical mechanisms of vertical heat transfer. Future research could
explore deep learning models that are capable of learning complex spatiotemporal
660 features and improving the physical interpretability of T_s variations across time, space,
and depth.

5. Conclusion

This study addresses the lack of high spatiotemporal resolution multi-layer T_s data by proposing a spatially adaptive ML framework, successfully constructing a retrieval model for multi-layer T_s . By integrating in-situ observations, reanalysis data, satellite remote sensing data, as well as topographic and soil texture data, the model demonstrates high accuracy across different depths, seasons, and land use types. The results indicate relatively higher performance in spring and autumn than in summer and winter, and greater accuracy in bare land, cropland, and grassland compared with forested areas. In comparison with ERA5-Land and GLDAS 2.1 T_s products, the multi-layer T_s data generated in this study exhibit significant improvements in both accuracy and spatial detail. Based on this framework, we have first developed the long-term (2010-2020) high spatiotemporal resolution (daily, 1 km resolution) multi-layer (0, 5, 10, 15, 20, 40 cm) T_s dataset for China. Future research could further explore methods that simultaneously integrate temporal, spatial, and depth information, and utilize multi-source sensor data to enhance the spatiotemporal monitoring capabilities of T_s at different depths. Overall, this study demonstrates the potential of multi-source data in T_s estimation and provides a reliable tool and data foundation for ecological modeling, agricultural production and related studies.

6. Data availability

The daily multi-layer T_s products (0, 5, 10, 15, 20, and 40 cm) at 1 km resolution from 2010 to 2020 are freely available in HDF5 format to the public at <https://doi.org/10.11888/Terre.tpd.302333> (Wang et al., 2025b). In addition, monthly multi-layer T_s data are also provided to meet the needs of various users.

Author contributions. XW, JM and HS developed the methodology and designed the experiments. LH and XW collected and processed the data. XW wrote the first draft of the paper under the supervision of other authors. All authors participated in the review and editing of the paper.

Competing interests. Author Hao Shi is a member of the editorial board of Earth System Science Data. The contact author has declared that no other competing interests are present.

695

Acknowledgments. We gratefully acknowledge the National Meteorological Center of the China Meteorological Administration for providing the observed T_s data. We thank the NASA Earth Observing System Data and Information System for providing MODIS and DEM data, and the European Centre for Medium-Range Weather Forecasts for the 700 ERA5-Land reanalysis dataset. We also acknowledge the Soil SubCenter of the National Earth System Science Data Center, National Science & Technology Infrastructure of China (<http://soil.geodata.cn>), for providing soil texture data. The flux tower data used for independent validation were provided by the ChinaFLUX network through the National Ecosystem Science Data Center, National Science & Technology 705 Infrastructure of China (<http://www.nesdc.org.cn>).

Financial support. This work was supported by the National Key Research and Development Program of China (Grant No. 2023YFF1303700) and the National 710 Natural Science Foundation of China (No. 42375195).

715

720

725

Reference

Akinwande, M. O., Dikko, H. G., and Samson, A.: Variance inflation factor: As a condition for the inclusion of suppressor variable(s) in regression analysis, *Open J. Stat.*, 5, 754–767, <https://doi.org/10.4236/ojs.2015.57075>, 2015.

730

Badache, M., Eslami-Nejad, P., Ouzzane, M., Aidoun, Z., and Lamarche, L.: A new modeling approach for improved ground temperature profile determination, *Renew. Energy*, 85, 436–444, <https://doi.org/10.1016/j.renene.2015.06.020>, 2016.

735

Bayatvarkeshi, M., Bhagat, S. K., Mohammadi, K., Kisi, O., Farahani, M., Hasani, A., Deo, R., and Yaseen, Z. M.: Modeling soil temperature using air temperature features in diverse climatic conditions with complementary machine learning models, *Comput. Electron. Agric.*, 185, 106158, <https://doi.org/10.1016/j.compag.2021.106158>, 2021.

740

Bond-Lamberty, B., Wang, C., and Gower, S. T.: Spatiotemporal measurement and modeling of stand-level boreal forest soil temperatures, *Agric. For. Meteorol.*, 131, 27–40, <https://doi.org/10.1016/j.agrformet.2005.04.008>, 2005.

745

Bright, R. M., Davin, E., O'Halloran, T., Pongratz, J., Zhao, K., and Cescatti, A.: Local temperature response to land cover and management change driven by non-radiative processes, *Nat. Clim. Change*, 7, 296–302, <https://doi.org/10.1038/NCLIMATE3250>, 2017.

Cao, R., Chen, Y., Shen, M., Chen, J., Zhou, J., Wang, C., and Yang, W.: A simple method to improve the quality of NDVI time-series data by integrating spatiotemporal information with the Savitzky-Golay filter, *Remote Sens. Environ.*, 217, 244–257, <https://doi.org/10.1016/j.rse.2018.08.022>, 2018.

750

Chen, L., Aalto, J., and Luoto, M.: Observed Decrease in Soil and Atmosphere Temperature Coupling in Recent Decades Over Northern Eurasia, *Geophys. Res. Lett.*, 48, e2021GL092500, <https://doi.org/10.1029/2021GL092500>, 2021a.

755

Chen, T. and Guestrin, C.: Xgboost: A scalable tree boosting system, in: *Proceedings of the 22nd ACM SIGKDD international conference on knowledge discovery and data mining*, 785–794, <https://doi.org/10.1145/2939672.2939785>, 2016.

Chen, X., Long, D., Hong, Y., Zeng, C., and Yan, D.: Improved modeling of snow and glacier melting by a progressive two-stage calibration strategy with GRACE and multisource data: How snow and glacier meltwater contributes to the runoff of the Upper Brahmaputra River basin?, *Water Resour. Res.*, 53, 2431–2466, <https://doi.org/10.1002/2016WR019656>, 2017.

760

Chen, Y., Cao, R., Chen, J., Liu, L., and Matsushita, B.: A practical approach to reconstruct high-quality Landsat NDVI time-series data by gap filling and the Savitzky–Golay filter, *ISPRS J. Photogramm. Remote Sens.*, 180, 174–190,

<https://doi.org/10.1016/j.isprsjprs.2021.08.015>, 2021b.

765 Cui, X., Xu, G., He, X., and Luo, D.: Influences of seasonal soil moisture and temperature on vegetation phenology in the Qilian Mountains, *Remote Sens.*, 14, 3645, <https://doi.org/10.3390/rs14153645>, 2022.

770 Duan, S.-B., Li, Z.-L., and Leng, P.: A framework for the retrieval of all-weather land surface temperature at a high spatial resolution from polar-orbiting thermal infrared and passive microwave data, *Remote Sens. Environ.*, 195, 107–117, <https://doi.org/10.1016/j.rse.2017.04.008>, 2017.

775 Fan, X., Zhang, Y., Shi, K., Peng, J., Liu, Y., Zhou, Y., Liu, Y., Zhu, Q., Song, C., Wan, R., Zhao, X., and Woolway, R. I.: Surging compound drought–heatwaves underrated in global soils, *Proc. Natl. Acad. Sci.*, 121, e2410294121, <https://doi.org/10.1073/pnas.2410294121>, 2024.

Farhangmehr, V., Imanian, H., Mohammadian, A., Cobo, J. H., Shirkhani, H., and Payeur, P.: A spatiotemporal CNN-LSTM deep learning model for predicting soil temperature in diverse large-scale regional climates, *Sci. Total Environ.*, 968, 178901, <https://doi.org/10.1016/j.scitotenv.2025.178901>, 2025.

780 Farr, T. G., Rosen, P. A., Caro, E., Crippen, R., Duren, R., Hensley, S., Kobrick, M., Paller, M., Rodriguez, E., Roth, L., Seal, D., Shaffer, S., Shimada, J., Umland, J., Werner, M., Oskin, M., Burbank, D., and Alsdorf, D.: The Shuttle Radar Topography Mission, *Rev. Geophys.*, 45, <https://doi.org/10.1029/2005RG000183>, 2007.

785 Feng, Y., Cui, N., Hao, W., Gao, L., and Gong, D.: Estimation of soil temperature from meteorological data using different machine learning models, *Geoderma*, 338, 67–77, <https://doi.org/10.1016/j.geoderma.2018.11.044>, 2019.

790 Firozjaei, M. K., Mijani, N., Kiavarz, M., Duan, S.-B., Atkinson, P. M., and Alavipanah, S. K.: A novel surface energy balance-based approach to land surface temperature downscaling, *Remote Sens. Environ.*, 305, 114087, <https://doi.org/10.1016/j.rse.2024.114087>, 2024.

795 Gao, Z., Lenschow, D. H., Horton, R., Zhou, M., Wang, L., and Wen, J.: Comparison of two soil temperature algorithms for a bare ground site on the Loess Plateau in China, *J. Geophys. Res. Atmospheres*, 113, <https://doi.org/10.1029/2008JD010285>, 2008.

Hong, F., Zhan, W., Götsche, F.-M., Liu, Z., Dong, P., Fu, H., Huang, F., and Zhang, X.: A global dataset of spatiotemporally seamless daily mean land surface temperatures: Generation, validation, and analysis, *Earth Syst. Sci. Data*, 14, 3091–3113, <https://doi.org/10.5194/essd-14-3091-2022>, 2022.

800 Hu, G., Zhao, L., Wu, X., Li, R., Wu, T., Xie, C., Qiao, Y., Shi, J., Li, W., and Cheng, G.: New Fourier-series-based analytical solution to the conduction–convection equation to calculate soil temperature, determine soil thermal properties, or estimate water flux, *Int. J. Heat Mass Transf.*, 95, 815–823, <https://doi.org/10.1016/j.ijheatmasstransfer.2015.11.078>, 2016.

805 Huang, R., Huang, J., Zhang, C., Ma, H., Zhuo, W., Chen, Y., Zhu, D., Wu, Q., and Mansaray, L. R.: Soil temperature estimation at different depths, using remotely-sensed data, *J. Integr. Agric.*, 19, 277–290, [https://doi.org/10.1016/S2095-3119\(19\)62657-2](https://doi.org/10.1016/S2095-3119(19)62657-2), 2020.

810 Huete, A., Didan, K., Miura, T., Rodriguez, E. P., Gao, X., and Ferreira, L. G.: Overview of the radiometric and biophysical performance of the MODIS vegetation indices, *Remote Sens. Environ.*, 83, 195–213, [https://doi.org/10.1016/S0034-4257\(02\)00096-2](https://doi.org/10.1016/S0034-4257(02)00096-2), 2002.

815 Hursh, A., Ballantyne, A., Cooper, L., Maneta, M., Kimball, J., and Watts, J.: The sensitivity of soil respiration to soil temperature, moisture, and carbon supply at the global scale, *Glob. Change Biol.*, 23, 2090–2103, <https://doi.org/10.1111/gcb.13489>, 2017.

820 Imanian, H., Mohammadian, A., Farhangmehr, V., Payeur, P., Goodarzi, D., Hiedra Cobo, J., and Shirkhani, H.: A comparative analysis of deep learning models for soil temperature prediction in cold climates, *Theor. Appl. Climatol.*, 155, 2571–2587, <https://doi.org/10.1007/s00704-023-04781-x>, 2024.

Jebamalar, A. S., Raja, S., and Bai, S.: Prediction of annual and seasonal soil temperature variation using artificial neural network, 9240 Lg 8435 I, 2012.

825 Karthikeyan, L. and Mishra, A. K.: Multi-layer high-resolution soil moisture estimation using machine learning over the United States, *Remote Sens. Environ.*, 266, 112706, <https://doi.org/10.1016/j.rse.2021.112706>, 2021.

830 Khosravi, K., Golkarian, A., Barzegar, R., Aalami, M. T., Heddam, S., Omidvar, E., Keesstra, S. D., and López-vicente, M.: Multi-step ahead soil temperature forecasting at different depths based on meteorological data: Integrating resampling algorithms and machine learning models, *Pedosphere*, 33, 479–495, <https://doi.org/10.1016/j.pedsph.2022.06.056>, 2023.

Kong, D., Zhang, Y., Gu, X., and Wang, D.: A robust method for reconstructing global MODIS EVI time series on the Google Earth Engine, *ISPRS J. Photogramm. Remote Sens.*, 155, 13–24, <https://doi.org/10.1016/j.isprsjprs.2019.06.014>, 2019.

835 Kropp, H., Loranty, M. M., Natali, S. M., Kholodov, A. L., Rocha, A. V., Myers-Smith, I., Abbot, B. W., Abermann, J., Blanc-Betes, E., Blok, D., Blume-Werry, G., Boike, J., Breen, A. L., Cahoon, S. M. P., Christiansen, C. T., Douglas, T. A., Epstein, H.

840 E., Frost, G. V., Goeckede, M., Høye, T. T., Mamet, S. D., O'Donnell, J. A., Olefeldt, D., Phoenix, G. K., Salmon, V. G., Sannel, A. B. K., Smith, S. L., Sonnentag, O., Vaughn, L. S., Williams, M., Elberling, B., Gough, L., Hjort, J., Lafleur, P. M., Euskirchen, E. S., Heijmans, M. M., Humphreys, E. R., Iwata, H., Jones, B. M., Jorgenson, M. T., Grünberg, I., Kim, Y., Laundre, J., Mauritz, M., Michelsen, A., Schaepman-Strub, G., Tape, K. D., Ueyama, M., Lee, B.-Y., Langley, K., and Lund, M.: Shallow soils are warmer under trees and tall shrubs across arctic and boreal ecosystems, *Environ. Res. Lett.*, 16, 015001, <https://doi.org/10.1088/1748-9326/abc994>, 2020.

845 Lembrechts, J. J., van den Hoogen, J., Aalto, J., Ashcroft, M. B., De Frenne, P., Kemppinen, J., Kopecký, M., Luoto, M., Maclean, I. M. D., Crowther, T. W., Bailey, J. J., Haesen, S., Klinges, D. H., Niittynen, P., Scheffers, B. R., Van Meerbeek, K., Aartsma, P., Abdalaze, O., Abedi, M., Aerts, R., Ahmadian, N., Ahrends, A., Alatalo, J. M., Alexander, J. M., Allonsius, C. N., Altman, J., Ammann, C., Andres, C., Andrews, C., Ardö, J., Arriga, N., Arzac, A., Aschero, V., Assis, R. L., Assmann, J. J., Bader, M. Y., Bahalkeh, K., Barančok, P., Barrio, I. C., Barros, A., Barthel, M., Basham, E. W., Bauters, M., Bazzichetto, M., Marchesini, L. B., Bell, M. C., Benavides, J. C., Benito Alonso, J. L., Berauer, B., Bjerke, J. W., Björk, R. G., Björkman, M. P., Björnsdóttir, K., Blonder, B., Boeckx, P., Boike, J., Bokhorst, S., Brum, B. N. S., Brůna, J., Buchmann, N., Buysse, P., Camargo, J. L., Campoe, O. C., Candan, O., Canessa, R., Cannone, N., Carbognani, M., Carnicer, J., Casanova-Katny, A., Cesár, S., Chojnicki, B., Choler, P., Chown, S. L., Cifuentes, E. F., Čiliak, M., Contador, T., Convey, P., Cooper, E. J., Cremonese, E., Curasi, S. R., Curtis, R., Cutini, M., Dahlberg, C. J., Daskalova, G. N., de Pablo, M. A., Della Chiesa, S., Dengler, J., Deronde, B., Descombes, P., Di Cecco, V., Di Musciano, M., Dick, J., Dimarco, R. D., Dolezal, J., Dorrepaal, E., Dušek, J., Eisenhauer, N., Eklundh, L., Erickson, T. E., et al.: Global maps of soil temperature, *Glob. Change Biol.*, 28, 3110–3144, <https://doi.org/10.1111/gcb.16060>, 2022.

860 Li, B., Liang, S., Ma, H., Dong, G., Liu, X., He, T., and Zhang, Y.: Generation of global 1 km all-weather instantaneous and daily mean land surface temperatures from MODIS data, *Earth Syst. Sci. Data*, 16, 3795–3819, <https://doi.org/10.5194/essd-16-3795-2024>, 2024a.

870 Li, N., Wang, L., and Chen, D.: Vegetation greening amplifies shallow soil temperature warming on the Tibetan Plateau, *Npj Clim. Atmospheric Sci.*, 7, 1–12, <https://doi.org/10.1038/s41612-024-00651-z>, 2024b.

875 Li, Q., Ma, M., Wu, X., and Yang, H.: Snow cover and vegetation-induced decrease in global albedo from 2002 to 2016, *J. Geophys. Res. Atmospheres*, 123, 124–138, <https://doi.org/10.1002/2017JD027010>, 2018.

Li, Q., Zhu, Y., Shangguan, W., Wang, X., Li, L., and Yu, F.: An attention-aware LSTM

model for soil moisture and soil temperature prediction, *Geoderma*, 409, 115651, <https://doi.org/10.1016/j.geoderma.2021.115651>, 2022.

880 Li, X., Zhu, Y., Li, Q., Zhao, H., Zhu, J., and Zhang, C.: Interpretable spatio-temporal modeling for soil temperature prediction, *Front. For. Glob. Change*, 6, 1295731, <https://doi.org/10.3389/ffgc.2023.1295731>, 2023a.

885 Li, X., Zhang, L., Wang, X., and Liang, B.: Forecasting greenhouse air and soil temperatures: A multi-step time series approach employing attention-based LSTM network, *Comput. Electron. Agric.*, 217, 108602, <https://doi.org/10.1016/j.compag.2023.108602>, 2024c.

Li, Y., Zeng, H., Zhang, M., Wu, B., Zhao, Y., Yao, X., Cheng, T., Qin, X., and Wu, F.: A county-level soybean yield prediction framework coupled with XGBoost and multidimensional feature engineering, *Int. J. Appl. Earth Obs. Geoinformation*, 118, 103269, <https://doi.org/10.1016/j.jag.2023.103269>, 2023b.

890 Liu, F., Wu, H., Zhao, Y., Li, D., Yang, J.-L., Song, X., Shi, Z., Zhu, A.-X., and Zhang, G.-L.: Mapping high resolution National Soil Information Grids of China, *Sci. Bull.*, 67, 328–340, <https://doi.org/10.1016/j.scib.2021.10.013>, 2022.

895 Liu X., Li Z.-L., Duan S.-B., Leng P., and Si M.: Retrieval of global surface soil and vegetation temperatures based on multisource data fusion, *Remote Sens. Environ.*, 318, 114564, <https://doi.org/10.1016/j.rse.2024.114564>, 2025.

Liu, Y., Liu, X., Fu, Z., Zhang, D., and Liu, L.: Soil temperature dominates forest spring phenology in China, *Agric. For. Meteorol.*, 355, 110141, <https://doi.org/10.1016/j.agrformet.2024.110141>, 2024.

900 Lloyd, J. and Taylor, J.: On the temperature dependence of soil respiration, *Funct. Ecol.*, 315–323, <https://doi.org/10.2307/2389824>, 1994.

Loranty, M. M., Berner, L. T., Goetz, S. J., Jin, Y., and Randerson, J. T.: Vegetation controls on northern high latitude snow-albedo feedback: Observations and CMIP 5 model simulations, *Glob. Change Biol.*, 20, 594–606, <https://doi.org/10.1111/gcb.12391>, 2014.

905 Mahanama, S. P. P., Koster, R. D., Reichle, R. H., and Suarez, M. J.: Impact of Subsurface Temperature Variability on Surface Air Temperature Variability: An AGCM Study, *J. Hydrometeorol.*, 9, 804–815, <https://doi.org/10.1175/2008JHM949.1>, 2008.

910 Mo, Y., Pepin, N., and Lovell, H.: Understanding temperature variations in mountainous regions: The relationship between satellite-derived land surface temperature and in situ near-surface air temperature, *Remote Sens. Environ.*, 318, 114574, <https://doi.org/10.1016/j.rse.2024.114574>, 2025.

915 Mortier, S., Hamedpour, A., Bussmann, B., Wandji, R. P. T., Latré, S., Sigurdsson, B. D., De Schepper, T., and Verdonck, T.: Inferring the relationship between soil temperature and the normalized difference vegetation index with machine learning, *Ecol. Inform.*, 82, 102730, 2024.

920 Muñoz-Sabater, J., Dutra, E., Agustí-Panareda, A., Albergel, C., Arduini, G., Balsamo, G., Boussetta, S., Choulga, M., Harrigan, S., Hersbach, H., Martens, B., Miralles, D. G., Piles, M., Rodríguez-Fernández, N. J., Zsoter, E., Buontempo, C., and Thépaut, J.-N.: ERA5-Land: a state-of-the-art global reanalysis dataset for land applications, *Earth Syst. Sci. Data*, 13, 4349–4383, <https://doi.org/10.5194/essd-13-4349-2021>, 2021.

925 Myers-Smith, I. H., Elmendorf, S. C., Beck, P. S. A., Wilmking, M., Hallinger, M., Blok, D., Tape, K. D., Rayback, S. A., Macias-Fauria, M., Forbes, B. C., Speed, J. D. M., Boulanger-Lapointe, N., Rixen, C., Lévesque, E., Schmidt, N. M., Baittinger, C., Trant, A. J., Hermanutz, L., Collier, L. S., Dawes, M. A., Lantz, T. C., Weijers, S., Jørgensen, R. H., Buchwal, A., Buras, A., Naito, A. T., Ravolainen, V., Schaepman-Strub, G., Wheeler, J. A., Wipf, S., Guay, K. C., Hik, D. S., and Vellend, M.: Climate sensitivity of shrub growth across the tundra biome, *Nat. Clim. Change*, 5, 887–891, <https://doi.org/10.1038/NCLIMATE2697>, 2015.

930 Nahvi, B., Habibi, J., Mohammadi, K., Shamshirband, S., and Al Razgan, O. S.: Using self-adaptive evolutionary algorithm to improve the performance of an extreme learning machine for estimating soil temperature, *Comput. Electron. Agric.*, 124, 150–160, <https://doi.org/10.1016/j.compag.2016.03.025>, 2016.

935 Ochsner, T. E., Horton, R., and Ren, T.: A new perspective on soil thermal properties, *Soil Sci. Soc. Am. J.*, 65, 1641–1647, <https://doi.org/10.2136/sssaj2001.1641>, 2001.

940 Peng, S., Ciais, P., Krinner, G., Wang, T., Gouttevin, I., McGuire, A. D., Lawrence, D., Burke, E., Chen, X., Decharme, B., and others: Simulated high-latitude soil thermal dynamics during the past 4 decades, *The Cryosphere*, 10, 179–192, 2016.

945 Rahman, M. H. ur, Ahmad, A., Wajid, A., Hussain, M., Rasul, F., Ishaque, W., Islam, Md. A., Shelia, V., Awais, M., Ullah, A., Wahid, A., Sultana, S. R., Saud, S., Khan, S., Fahad, S., Hussain, M., Hussain, S., and Nasim, W.: Application of CSM-CROPGRO-cotton model for cultivars and optimum planting dates: Evaluation in changing semi-arid climate, *Field Crops Res.*, 238, 139–152, <https://doi.org/10.1016/j.fcr.2017.07.007>, 2019.

950 Shati, F., Prakash, S., Norouzi, H., and Blake, R.: Assessment of differences between near-surface air and soil temperatures for reliable detection of high-latitude freeze and thaw states, *Cold Reg. Sci. Technol.*, 145, 86–92, <https://doi.org/10.1016/j.coldregions.2017.10.007>, 2018.

Smith, S. L., O'Neill, H. B., Isaksen, K., Noetzli, J., and Romanovsky, V. E.: The changing thermal state of permafrost, *Nat. Rev. Earth Environ.*, 3, 10–23, <https://doi.org/10.1038/s43017-021-00240-1>, 2022.

955 Wan, Z. and Dozier, J.: A generalized split-window algorithm for retrieving land-surface temperature from space, *IEEE Trans. Geosci. Remote Sens.*, 34, 892–905, <https://doi.org/10.1109/36.508406>, 1996.

Wang, D., Wang, A., and Wang, Z.: A multilayer daily high-resolution gridded homogenized soil temperature over continental China, *Int. J. Climatol.*, 43, 2015–2030, <https://doi.org/10.1002/joc.7959>, 2023.

960 Wang, K. and Dickinson, R. E.: Contribution of solar radiation to decadal temperature variability over land, *Proc. Natl. Acad. Sci.*, 110, 14877–14882, <https://doi.org/10.1073/pnas.1311433110>, 2013.

965 Wang, M., Wang, Y., Liu, X., Hou, W., Wang, J., Li, S., Zhao, L., and Hu, Z.: Vapor pressure deficit dominates vegetation productivity during compound drought and heatwave events in China's arid and semi-arid regions: Evidence from multiple vegetation parameters, *Ecol. Inform.*, 88, 103144, <https://doi.org/10.1016/j.ecoinf.2025.103144>, 2025a.

970 Wang, Q., Tang, Y., Tong, X., and Atkinson, P. M.: Filling gaps in cloudy landsat LST product by spatial-temporal fusion of multi-scale data, *Remote Sens. Environ.*, 306, 114142, <https://doi.org/10.1016/j.rse.2024.114142>, 2024.

Wang, X., He, L., Shi, H., and Yu, Q.: Daily multi-layer soil temperature dataset with 1 km resolution in China from 2010 to 2020, <https://doi.org/10.11888/Terre.tpdc.302333>, 2025b.

975 Wu, P., Su, Y., Duan, S., Li, X., Yang, H., Zeng, C., Ma, X., Wu, Y., and Shen, H.: A two-step deep learning framework for mapping gapless all-weather land surface temperature using thermal infrared and passive microwave data, *Remote Sens. Environ.*, 277, 113070, <https://doi.org/10.1016/j.rse.2022.113070>, 2022.

980 Xing, L., Li, L., Gong, J., Ren, C., Liu, J., and Chen, H.: Daily soil temperatures predictions for various climates in United States using data-driven model, *Energy*, 160, 430–440, <https://doi.org/10.1016/j.energy.2018.07.004>, 2018.

Xu, C., Qu, J. J., Hao, X., Zhu, Z., and Gutenberg, L.: Surface soil temperature seasonal variation estimation in a forested area using combined satellite observations and in-situ measurements, *Int. J. Appl. Earth Obs. Geoinformation*, 91, 102156, <https://doi.org/10.1016/j.jag.2020.102156>, 2020.

985 Xu, C., Liao, S., Huang, L., and Xia, J.: Soil temperature estimation at different depths over the central Tibetan Plateau integrating multiple Digital Earth observations

and geo-computing, *Int. J. Digit. Earth*, 16, 4023–4043, <https://doi.org/10.1080/17538947.2023.2264267>, 2023.

990 Xu, S., Fu, Q., Li, T., Meng, F., Liu, D., Hou, R., Li, M., and Li, Q.: Spatiotemporal characteristics of the soil freeze-thaw state and its variation under different land use types - A case study in Northeast China, *Agric. For. Meteorol.*, 312, 108737, <https://doi.org/10.1016/j.agrformet.2021.108737>, 2022.

995 Yamamoto, Y., Ichii, K., Ryu, Y., Kang, M., and Murayama, S.: Uncertainty quantification in land surface temperature retrieved from Himawari-8/AHI data by operational algorithms, *ISPRS J. Photogramm. Remote Sens.*, 191, 171–187, <https://doi.org/10.1016/j.isprsjprs.2022.07.008>, 2022.

1000 Yang, K. and Zhang, J.: Evaluation of reanalysis datasets against observational soil temperature data over China, *Clim. Dyn.*, 50, 317–337, <https://doi.org/10.1007/s00382-017-3610-4>, 2018.

1005 You, W., Huang, C., Hou, J., Zhang, Y., Dou, P., and Han, W.: Reconstruction of MODIS LST Under Cloudy Conditions by Integrating Himawari-8 and AMSR-2 Data Through Deep Forest Method, *IEEE Trans. Geosci. Remote Sens.*, 62, 1–17, <https://doi.org/10.1109/TGRS.2024.3388409>, 2024.

Zhang, T.: Influence of the seasonal snow cover on the ground thermal regime: An overview, *Rev. Geophys.*, 43, <https://doi.org/10.1029/2004RG000157>, 2005.

1010 Zhang, Y., Chen, W., Smith, S. L., Riseborough, D. W., and Cihlar, J.: Soil temperature in Canada during the twentieth century: Complex responses to atmospheric climate change, *J. Geophys. Res. Atmospheres*, 110, <https://doi.org/10.1029/2004JD004910>, 2005.

1015 Zhao, T., Liu, S., Xu, J., He, H., Wang, D., Horton, R., and Liu, G.: Comparative analysis of seven machine learning algorithms and five empirical models to estimate soil thermal conductivity, *Agric. For. Meteorol.*, 323, 109080, <https://doi.org/10.1016/j.agrformet.2022.109080>, 2022.